

Visiting Scientist mission report

Document NWP_AVS22_01

Version 1.0

18.08.2022

Cloud particle orientation and polarisation for cross-track microwave sensors in RTTOV

Vasileios Barlakas¹, Alan J. Geer², Patrick Eriksson¹

¹*Chalmers University of Technology, Department of Space, Earth and Environment, Gothenburg, Sweden*

²*ECMWF, Research Department, Shinfield Park, Reading, RG2 9AX, UK*





Cloud particle orientation
and polarisation for cross-
track microwave sensors in
RTTOV

Doc ID : NWPSAF-EC_VS-061
Version : 1.0
Date : 18.08.2022

Cloud particle orientation and polarisation for cross-track microwave sensors in RTTOV

Vasileios Barlakas¹, Alan J. Geer², Patrick Eriksson¹

¹*Chalmers University of Technology, Department of Space, Earth and Environment, Gothenburg, Sweden*

²*ECMWF, Research Department, Shinfield Park, Reading, RG2 9AX, UK*

This documentation was developed within the context of the EUMETSAT Satellite Application Facility on Numerical Weather Prediction (NWP SAF), under the Cooperation Agreement dated 7 September 2021, between EUMETSAT and the Met Office, UK, by one or more partners within the NWP SAF. The partners in the NWP SAF are the Met Office, ECMWF, DWD and Météo France.

Copyright 2022, EUMETSAT, All Rights Reserved.

Change record			
Version	Date	Author / changed by	Remarks
0.1	27.07	V. Barlakas	Draft version
0.2	29.07	V. Barlakas	Incorporated comments from A. Geer
0.3	15.08	A. Geer	Small changes and suggestions
1.0	18.08	V. Barlakas	Final version

Cloud particle orientation and polarisation for cross-track microwave sensors in RTTOV

Vasileios Barlakas¹, Alan J. Geer², and Patrick Eriksson¹

¹Department of Space, Earth and Environment, Chalmers University of Technology, Gothenburg, Sweden

²ECMWF, Research Department, Shinfield Park, Reading, RG2 9AX, UK

Abstract. This report summarises the work conducted during the associate scientist mission NWPSAF_AS22_01; accounts are given for the period 01.04.2022-31.05.2022. The objective of this mission was to provide a more comprehensive capability for modelling oriented ice particles in RTTOV-SCATT, the microwave (MW) and sub-millimetre (sub-mm) scattering component of RTTOV. This provides more accurate simulations of cloud and precipitation-affected radiances and extends the capability to represent orientation and polarisation to cross-track sensors. Reducing errors in forward modelling could improve the quality of the initial conditions for weather forecasting and ultimately improve weather forecasts.

1 Introduction

The Radiative Transfer for TIROS Operational Vertical Sounder model (RTTOV, e.g., Saunders et al., 2018) is able to simulate cloud and precipitation-affected radiances from microwave sensors (RTTOV-SCATT, Bauer et al., 2006) with sufficient accuracy (e.g., Barlakas et al., 2022) that they can be used for all-sky assimilation in weather forecasting (Geer et al., 2017) and for validating and improving forecast models of cloud and precipitation (Forbes et al., 2016). Underpinning these simulations are optical properties from scattering databases representing non-spherical frozen hydrometeors, such as pristine ice, snow, aggregates and hail.

In the majority, scattering databases are solely comprised by totally randomly oriented (TRO) hydrometeors. Such hydrometeors, regardless their non-spherical shapes, barely induce any polarisation signature. To elaborate, former studies showed that non-spherical TRO hydrometeors induce only limited polarisation signal (up to about 1 K) in the MW and sub-mm part of the spectrum (Emde et al., 2004; Davis et al., 2005; Brath et al., 2020; Barlakas et al., 2021). This can be attributed to the nature of TRO, which results in no dichroism effect (the extinction cross section for linear polarisation is zero) and any induced polarisation is due to scattering effects (Emde et al., 2004; Davis et al., 2005; Teichmann et al., 2006; Barlakas et al., 2016a).

In nature, frozen cloud and precipitation hydrometeors are often preferentially oriented, and they generally exhibit azimuthally random orientation (ARO, Brath et al., 2020). This concept means that the hydrometeors have no preferred orientation in the azimuth direction, but they do have a preferred distribution in angle between the reference plane of the hydrometeor and the horizon; for details, the reader is referred to Brath et al. (2020); Barlakas et al. (2021). Compared to TRO, ARO hydrometeors are characterized by a strong dichroism effect and hence, they induce V – H polarisation differences (PD). This effect is believed to be responsible for observed polarisation differences of up to about 15 K in magnitude observed with con-

ically scanning microwave imagers, which are seen globally, almost anywhere there are frozen hydrometeors (e.g., Gong and Wu, 2017; Galligani et al., 2021; Barlakas et al., 2021). Any single channel on a microwave sensor measures a single linear polarisation, which means that brightness temperature T_B simulations made without consideration of scattering-induced polarisation are routinely in error by up to 7.5 K due to the unrepresented V – H polarisation differences. The presence of ARO particles also change the mean scattering properties (e.g., Barlakas et al., 2021; Kaur et al., 2022) and any simulation neglecting such behavior may be even further in error. The representation of preferentially oriented particles has only recently been recognised as one of the most important remaining errors in radiative transfer modelling. From a climate science perspective, particle orientation in ice clouds is also important to radiative transfer at visible and infrared frequencies (e.g., Saito and Yang, 2019), thereby giving added incentive to understand hydrometeor orientation using instruments like the upcoming Ice Cloud Imager mission that will operate at sub-mm frequencies.

The lack of scattering databases with ARO hydrometeors has been one of the main reasons why polarisation has been neglected from radiative transfer applications in the MW and sub-mm, i.e. retrievals and data assimilation (DA). In addition, preferentially oriented hydrometeors require more sophisticated radiative transfer solvers, substantially increasing the required computation time and making them unaffordable for DA applications (e.g., Davis et al., 2005; Barlakas et al., 2021, and references therein). Only recently, approaches to approximate the ARO hydrometeors have been explored (Galligani et al., 2021; Barlakas et al., 2021); but their application is limited to conical scanning radiometers. Galligani et al. (2021) suggested a scheme for parameterizing the polarisation signatures observed from Global Precipitation Mission microwave imager (GMI) at 89.0 and 166.0. Still their approach is restricted to dual-polarisation observations. A more physically based scheme was developed by Barlakas et al. (2021). It is based on rescaling the layer optical thickness of TRO hydrometeors to approximate the differences between V and H in case of ARO hydrometeors (dichroism effect). This is quantified by the so-called polarisation ratio ρ .

The scheme by Barlakas et al. (2021) was implemented in RTTOV-SCATT and successfully tested in the Integrated Forecast System (IFS) of the European Centre for Medium-Range Weather Forecasts (ECMWF). It can effectively simulate V – H PDs in the case of conically scanning radiometers. As well as mostly removing the errors in V – H differences for the same sensor, it gives a more consistent overall assimilation of sensors such as GMI and the Special Sensor Microwave Imager/Sounder (SSMIS), since these instruments have different polarisations at some frequencies (and hence could differ by up to 15 K when making observations of the same cloud). Barlakas et al. (2021) found that a ρ value of 1.4 best represents the orientation of frozen hydrometeors in RTTOV-SCATT and the IFS; this factor was applied to all frozen species and at all channels. For details on the scheme and its performance, the reader is referred to Barlakas et al. (2021).

Modeling the effects of oriented frozen hydrometeors on the basis of cross-track scanners is much more complicated, since the bulk optical properties strongly depend on the Earth incident angle. Furthermore, in cross-track scanners, polarisation rotates with the observation angle of the sensor, increasing the level of complexity. Here, an improved parameterisation is proposed for approximating the polarisation effects of ARO hydrometeors and reproducing the observed polarisation signal from cross-track scanners. Unlike the previous empirical scheme (Barlakas et al., 2021), the new approach is based on simulated ARO particles, and it represents the changes in mean scattering properties as well as the polarisation differences. This scheme is

validated against full polarisation simulations (ARO) by means of the reference quality model ARTS (Atmospheric Radiative Transfer Simulator, Buehler et al., 2005) for frequencies between 89.0 and about 190.31 GHz. This scheme is intended to supersede the earlier parameterisation, which was introduced in RTTOV version 13 (hereafter v13.0). A parameterization for radar backscattering is also developed.

2 Methods and tools

2.1 Hydrometeor orientation

Frozen hydrometeors are characterised by non-spherical shapes. Consequently, they can be preferentially oriented owing to aerodynamical and/or gravitational forces (e.g., Khvorostyanov and Curry, 2014; Brath et al., 2020). Accordingly, preferentially oriented hydrometeors are characterised by the so-called dichroism effect, meaning viewing dependent scattering and absorption properties (optical properties, Davis et al., 2005; Brath et al., 2020). This means that instruments (microwave imagers and sounders) equipped with channels characterised by different polarisations will observe different optical properties.

In radiative transfer theory, the scattering of the electromagnetic radiation due to the presence of a hydrometeor is described by the scattering matrix:

$$\mathbf{Z} = \begin{bmatrix} Z_{11} & Z_{12} & Z_{13} & Z_{14} \\ Z_{21} & Z_{22} & Z_{23} & Z_{24} \\ Z_{31} & Z_{32} & Z_{33} & Z_{34} \\ Z_{41} & Z_{42} & Z_{43} & Z_{44} \end{bmatrix}. \quad (1)$$

\mathbf{Z} depends on the incident ("inc") and the scattering ("sca") directions, described by the zenithal (θ) and azimuth (ϕ) angles and the orientation of the hydrometeor. The scattering matrix is applied to the four-element Stokes vector representation of the electromagnetic (EM) radiation (see appendix A). In addition, the attenuation between the hydrometeor and the incident EM radiation is described by a 4 x 4 extinction matrix:

$$\mathbf{K} = \begin{bmatrix} K_{11} & K_{12} & K_{13} & K_{14} \\ K_{21} & K_{22} & K_{23} & K_{24} \\ K_{31} & K_{32} & K_{33} & K_{34} \\ K_{41} & K_{42} & K_{43} & K_{44} \end{bmatrix}. \quad (2)$$

\mathbf{K} depends on the incident direction and the orientation of the hydrometeor (e.g., Barlakas, 2016; Brath et al., 2020) with regard to the chosen frame of reference (known as the laboratory system in these works). The orientation of the hydrometeor with respect to the laboratory system is typically described by the three Euler angles: $\alpha \in [0, 2\pi]$, $\beta \in [0, \pi]$, and $\gamma \in [0, 2\pi]$ (see Fig. 1). For details on the various coordinate systems, the reader is referred to (Brath et al., 2020; Barlakas et al., 2021).

Taking inspiration from observed hydrometeor distributions, the optical properties of hydrometeors of a particular size and shape are represented by an ensemble of particles with different orientations. In practice, one needs to average the single scattering properties over all orientations to obtain the ensemble equivalent single scattering properties (Mishchenko and Yurkin,

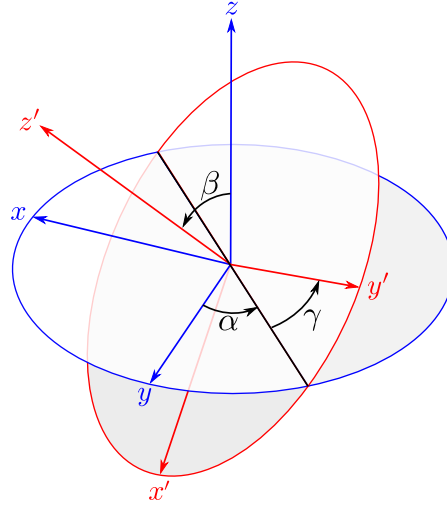


Figure 1. Euler angles. Figure is adopted from Brath et al. (2020).

2017):

$$\langle \psi \rangle = \int_0^{2\pi} \int_0^{\pi} \int_0^{2\pi} p(\alpha) \cdot p(\beta) \cdot p(\gamma) \cdot \psi d\alpha d\beta d\gamma, \quad (3)$$

where ψ is a single scattering property, i.e. scattering matrix, extinction matrix, absorption vector) at a specific orientation, and $p(\alpha)$, $p(\beta)$, and $p(\gamma)$ denote the probability distributions of the three Euler angles, respectively.

For TRO hydrometeors, α , β , and γ are uniformly distributed, meaning that all orientations are equally possible. As a result, \mathbf{K} is independent of the incoming and outgoing directions and has only one non-zero element, i.e. $K_{\text{TRO}} = K_{11}$; the extinction cross section. Similarly, the scattering matrix is reduced to its first element:

$$Z_{\text{TRO}}(\Theta) = Z_{11}(\theta_{\text{inc}}, \phi_{\text{inc}}, \theta_{\text{sca}}, \phi_{\text{sca}}), \quad (4)$$

that is the so-called phase function, with Θ being the scattering angle described by:

$$\cos\Theta = \cos\theta_{\text{inc}} \cdot \cos\theta_{\text{sca}} + \sin\theta_{\text{inc}} \cdot \sin\theta_{\text{sca}} \cdot \cos(\phi_{\text{sca}} - \phi_{\text{inc}}). \quad (5)$$

ARO hydrometeors describe a preferred orientation to the horizon (no preference in the azimuth direction) as is expected to develop due to aerodynamical and/or gravitational forces. In brief, by aligning the laboratory z axis along the direction of the force, α and γ are uniformly distributed, and the only degree of freedom is the tilt angle β (Mishchenko et al., 1999; Brath et al., 2020). Accordingly, from Eq. (3), the expressions for the scattering and extinction matrices on the basis of ARO are:

$$\mathbf{Z}_{\text{ARO}}(\theta_{\text{inc}}, \theta_{\text{sca}}, \phi_{\text{sca}}, \beta) = \int_0^{2\pi} \int_0^{2\pi} p(\alpha) \cdot p(\gamma) \cdot \mathbf{Z}(\theta_{\text{inc}}, \phi_{\text{inc}} = 0, \theta_{\text{sca}}, \phi_{\text{sca}}, \alpha, \beta, \gamma) d\alpha d\gamma \quad (6)$$

and

$$\mathbf{K}_{\text{ARO}}(\theta_{\text{inc}}, \beta) = \int_0^{2\pi} \int_0^{2\pi} p(\alpha) \cdot p(\gamma) \cdot \mathbf{K}(\theta_{\text{inc}}, \phi_{\text{inc}} = 0, \alpha, \beta, \gamma) d\alpha d\gamma. \quad (7)$$

Note here that, due to the orientation averaging, \mathbf{Z}_{ARO} depends on the relative azimuth angle, i.e. $\Delta\phi = \phi_{\text{inc}} - \phi_{\text{sca}}$. For simplicity, ϕ_{inc} is set to 0 in case of ARO (Brath et al., 2020). In addition, due to the axial symmetry Eq. 8 has only three independent elements:

$$\mathbf{K}_{\text{ARO}} = \begin{bmatrix} K_{11} & K_{12} & 0 & 0 \\ K_{12} & K_{11} & 0 & 0 \\ 0 & 0 & K_{11} & K_{34} \\ 0 & 0 & -K_{34} & K_{11} \end{bmatrix}. \quad (8)$$

K_{12} and K_{34} are the cross section for linear and circular polarisation, respectively. In other words, the former describes the differences in the extinction between V- and H-polarisation, while the latter denotes the differences in the extinction between $+45^\circ$ and -45° polarization.

2.2 Optical properties in RTTOV-SCATT

For representing scattering in an operational model like RTTOV-SCATT, one needs to supply the extinction, the asymmetry parameter (g), the backscatter coefficient b , and the single scattering albedo (ω). RTTOV-SCATT considers TRO hydrometeors; hence, the extinction is given by $K_{\text{TRO}} = K_{11}$ (see Section 2.1).

The asymmetry parameter is a measure for the preferred scattering direction and ranges between -1 (backscattering) and $+1$ (forward scattering), with a g value of zero indicating an equal preferred forward and backward directions. The formulations for TRO and ARO are:

$$g_{\text{TRO}} = \frac{\int_0^{2\pi} d\phi \int_0^\pi Z_{\text{TRO}} \cdot \cos(\Theta) \sin(\Theta) d\Theta}{\int_0^{2\pi} d\phi \int_0^\pi Z_{\text{TRO}} \cdot \sin(\Theta) d\Theta}, \quad (9)$$

$$g_{\text{ARO}}(\theta_{\text{inc}}, \beta) = \frac{\int_0^{2\pi} \int_0^\pi Z_{\text{ARO},11}(\theta_{\text{inc}}, \theta_{\text{sca}}, \phi_{\text{sca}}, \beta) \cdot \cos(\theta) \sin(\theta) d\theta d\phi}{\int_0^{2\pi} \int_0^\pi Z_{\text{ARO},11}(\theta_{\text{inc}}, \theta_{\text{sca}}, \phi_{\text{sca}}, \beta) \cdot \sin(\theta) d\theta d\phi},$$

Recall here that, in case of ARO, the scattering and the extinction matrix are defined in the laboratory system. Accordingly, before the derivation of g_{ARO} , one needs to transform the laboratory system to the incident-direction-related coordinate system. For details on the transformations between the coordinate systems, the reader is referred to Brath et al. (Appendix D; 2020).

For simulating radar measurements (only at nadir), the key component is the backscattering. It is essentially the scattering matrix value for the backward direction:

$$b_{\text{TRO}} = Z_{\text{TRO}}(\Theta = \pi), \quad (10)$$

$$b_{\text{ARO}}(\beta) = Z_{\text{ARO},11}(\theta_{\text{inc}} = \pi, \theta_{\text{sca}} = 0, \phi_{\text{sca}} = 0, \beta).$$

Finally, the single scattering albedo is derived as follows:

$$\omega_{\text{TRO}} = \frac{\int_0^{2\pi} d\phi \int_0^\pi Z_{\text{TRO}} \cdot \sin(\Theta) d\Theta}{K_{\text{TRO}}}, \quad (11)$$

$$\omega_{\text{ARO}}(\theta_{\text{inc}}, \beta) = \frac{\int_0^{2\pi} \int_0^\pi Z_{\text{ARO},11}(\theta_{\text{inc}}, \theta_{\text{sca}}, \phi_{\text{sca}}) \cdot \sin(\theta) d\theta d\phi}{K_{\text{ARO},11}(\theta_{\text{inc}}, \beta)}.$$

Note here that, in case of ARO, the above equations describe the scenario with no preferred polarisation. For the formulas at pure V- and H-polarisation, there reader is referred to the Appendix A.

In this initial parameterisation, as in previous work, the optical properties used in RTTOV-SCATT are identical in both the solution of the delta-Eddington radiative transfer equation and also in the line-of-sight integration. The chosen ARO optical properties are appropriate to the line-of-sight integration, so that θ_{inc} is equated to the earth incident angle of the line-of-sight. However, it is possible that different and more optimal optical properties could be chosen for the delta-Eddington integration, which represents integrated scattering across all incident angles (see also Appendix A). This will be the subject of future work.

2.3 Microphysical configuration

Accurate radiative transfer simulations require realistic representations of the shape, size distribution, and orientation of the hydrometeors.

Towards this direction, the ARTS scattering database has been employed that consists of both TRO (Eriksson et al., 2018) and ARO (Brath et al., 2020) hydrometeors. Currently, a total of 35 habits in TRO are included as well as two additional habits in ARO (i.e. large plate aggregate and plate type for various tilt angles), excluding habits in liquid phase. The database offers the single scattering properties at 34 frequencies (1.0–886.0 GHz) and at three temperatures (190, 230, and 270 K). The TRO habits are available in at least 34 sizes per habit, while the ARO at 19 sizes. Herein, the large plate aggregate (LPA) habit has been employed for both TRO and ARO hydrometeors. For the latter, a tilt angle of 0° is utilized, since this value was found to recreate best dual-polarisation MW observations (Brath et al., 2020).

The above selection is considered a good microphysical representation for non-spherical frozen hydrometeors in the MW (Brath et al., 2020; Geer, 2021). Ideally, the microphysical choice would be situation dependent. However, this would increase the intricacy of the forward operator and further complicates any attempts to impartially certify the impact of any parameterisation.

To avoid any inconsistencies between ARO and TRO due to the differences in the available sizes, we decided not to use the TRO from Eriksson et al. (2018), but to derive them from the ARO ones simply by integrating over all the tilted angles:

$$K_{\text{TRO}} = \int_0^{\pi/2} p(\beta) \cdot K_{\text{ARO},11}(\theta_{\text{inc}}, \beta) d\beta. \quad (12)$$

The tilt angles above 90° have been skipped, due to the fact that LPA has a mirror symmetry around $\theta_{\text{inc}} = 90^\circ$. The scattering matrix is derived in a similar way.

2.4 Bulk optical properties

The bulk optical properties are derived by integrating the single scattering properties over the PSD. To exemplify, for a given particle size distribution $N(D_q)$, with D_q describing the geometric diameter, the bulk extinction is given by:

$$k_{\text{TRO}} = \int_{D_{\text{min}}}^{D_{\text{max}}} K_{\text{TRO}}(D_q) \cdot N(D_q) dD_q, \quad (13)$$

$$k_{\text{ARO}}(\theta_{\text{inc}}, \beta) = \int_{D_{\text{min}}}^{D_{\text{max}}} K_{\text{ARO},11}(D_q, \theta_{\text{inc}}, \beta) \cdot N(D_q) dD_q.$$

Similar equations are derived for the other optical properties, i.e. g , ω , and b . The PSD is fitted to a particular water content and hence the bulk optical properties are dependent on water content (as well as on frequency and temperature); a comprehensive description for the derivation of the bulk properties in RTTOV-SCATT is found in Geer et al. (2021).

2.5 Polarisation parameterisation

Figure 2 depicts the differences in the bulk optical properties between ARO and TRO as a function of the frozen water content (wc) for various θ_{inc} (introduced in Section 2.1) at both V- (upper panels) and H-polarisation (lower panels). Here, we should clarify that θ_{inc} can be seen as the angle that the line-of-sight of the satellite falls on the Earth surface, i.e. the Earth incident angle. Details on the derivation of the bulk properties for ARO for pure V- and H-polarisation are found in Appendix A.

In Fig. 2, one can clearly see that the bulk extinction and the asymmetry parameter (at both V and H) have a strong dependence to both θ_{inc} and wc; orientation of non-spherical frozen hydrometeors induces differences that can be as large as 40% and 60–80% in k and g , respectively, especially at low values of wc and both nadir and 75° (the largest observation angle of current cross track scanners). On the contrary, hydrometeor orientation has only a limited impact on the single scattering albedo (see Fig. 2c and 2f). Note here that these patterns are characterised by a strong dependency on the frequency, especially at sub-mm frequencies (above about 240 GHz), and a low dependency on the temperature (not shown here). At about 55° (conical scanning radiometers), in addition to ω , g is also marginally impacted by hydrometeor orientation (see black dashed lines in Fig. 2b and 2e). In other words, ARO and TRO properties at about 55° are fairly similar, with the only exception being the extinction at both V- and H-polarisation (see Fig. 2a and 2d). This special characteristic enabled the empirical quantification of the differences in extinction between V- and H-polarisation and led to the current parametrisation in RTTOV (Barlakas et al., 2021).

To that end, to model the effects of ARO frozen hydrometeors in recreating the observed polarisation signal from cross-track scanners, a frequency-, temperature-, angular-, and water content-dependent scaling factor is required, which is defined as follows:

$$\rho_\beta = \frac{\beta_{\text{ARO}}}{\beta_{\text{TRO}}}, \quad (14)$$

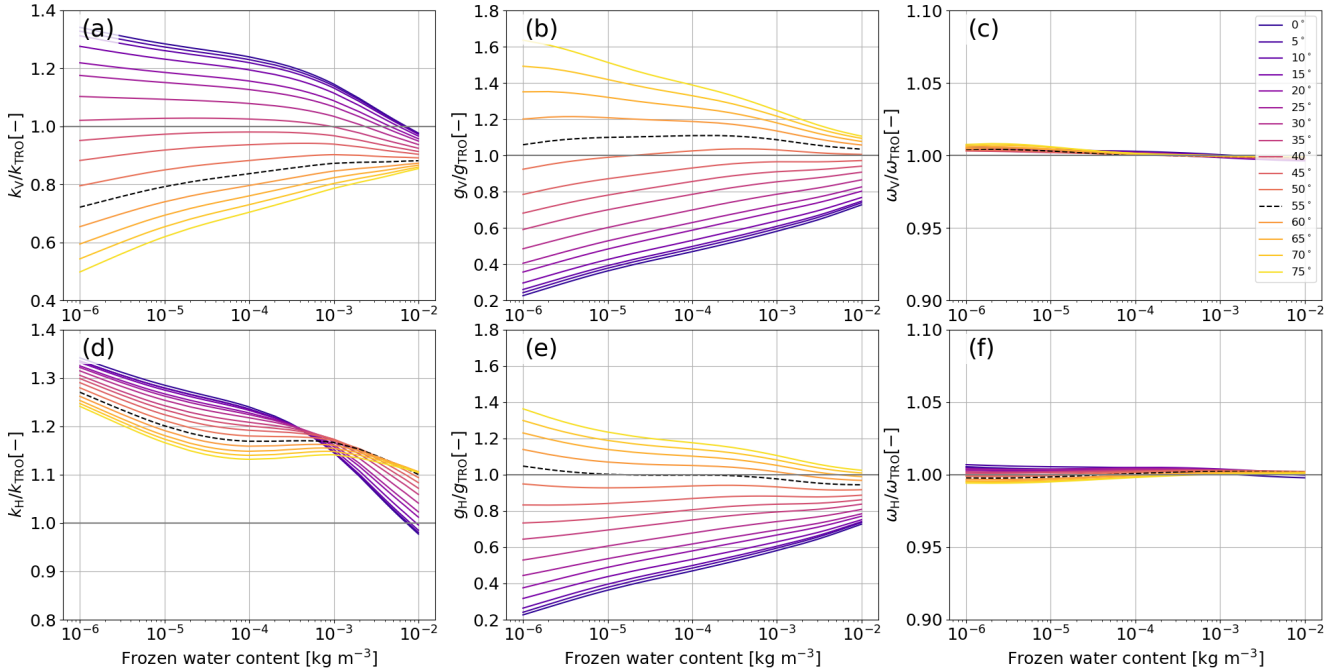


Figure 2. For the large plate aggregate and the particle size distribution of Field et al. (2007) (tropical configuration), bulk optical properties of azimuth random orientation (ARO) at both V and H polarisation normalized by the corresponding properties in case of total random orientation (TRO) as a function of the frozen water content. Results are presented at 230 K for various incident angles (θ_{inc} ; highlighted by the different colors) at 166.9 GHz on the basis of the extinction (K), the asymmetry parameter (g) and the single scattering albedo (ω). The black dashed line denote the typical observation angle of conical scanning radiometers ($\approx 55^\circ$). For ARO, the single scattering properties for a tilt angle of 0° are employed (Brath et al., 2020).

where β_{ARO} and β_{TRO} are the bulk optical properties for ARO and TRO, respectively (see Appendix A). Basically, Fig. 2 depicts the ρ for a temperature of 230 K and a frequency of 166.9 GHz. The scheme is implemented by means of a four-dimensional (4D) lookup table (LUT) that will be applied to the bulk scattering optical properties in case of TRO. Although ω is only marginally affected by orientation, we decided to include it for completeness.

To sum up, the 4D LUT is comprised of scaling factors for k , g , ω , and radar backscattering (b) at both V- and H-polarisations. Note here that, for the time being, b is valid only at nadir, and it has not been validated yet.

3 Considering the rotation of polarisation with the scan angle of the instrument

In cross-track instruments, the antenna of the sensor scans across from a limb position to nadir and then to a limb position on the other side. This is achieved by orienting the antenna at 45 degrees to the earth nadir and by rotating it around an axis typically aligned with the spacecraft direction of travel. The feedhorns used to measure the signal from the antenna are also aligned along the spacecraft direction of travel and measure a fixed polarisation. Consequently, an instrument collecting signals

from V- or H-polarisation at nadir will be measuring a rotated polarisation at other scan angles. This results in what is known as, respectively, a quasi-V and quasi-H polarisation signature. To model the effect of ARO frozen hydrometeors in recreating the observed polarisation signal from cross-track scanners, the rotation of polarisation with the scan angle of the sensor needs to be taken into account. The scan angle is linked to θ_{inc} as follows:

$$\theta_s = \arcsin\left(\frac{R}{R+H} \cdot \sin(\pi - \theta_{\text{inc}})\right), \quad (15)$$

where R and H are the Earth radius and the altitude of the satellite, respectively. Accordingly, the bulk optical properties (b) seen by a cross-track instrument are given by:

$$\begin{aligned} \beta^{\text{QV}} &= \varrho_{\beta}^{\text{V}}(\theta_{\text{inc}}) \cdot \beta^{\text{V}} \cdot \cos^2(\theta_s) + \varrho_{\beta}^{\text{H}}(\theta_{\text{inc}}) \cdot \beta^{\text{H}} \cdot \sin^2(\theta_s), \\ \beta^{\text{QH}} &= \varrho_{\beta}^{\text{V}}(\theta_{\text{inc}}) \cdot \beta^{\text{V}} \cdot \sin^2(\theta_s) + \varrho_{\beta}^{\text{H}}(\theta_{\text{inc}}) \cdot \beta^{\text{H}} \cdot \cos^2(\theta_s). \end{aligned} \quad (16)$$

Where β^{V} and β^{H} are the bulk properties (k , g , ω , and b) at pure V- and H-polarisation, $\varrho_{\beta}^{\text{V}}$ and $\varrho_{\beta}^{\text{H}}$ are the corresponding scaling factors, while β^{QV} and β^{QH} are the bulk properties for quasi-V and quasi-H polarisation. Depending on the polarisation of the channels at nadir, one should consider one of the above equations. Note that since the TRO optical properties are invariant with polarisation, in the current scheme $\beta^{\text{V}} = \beta^{\text{H}}$.

4 Simulation setup

The evaluation of the polarisation parameterisation in RTTOV-SCATT was conducted by means of ARTS. Towards this direction, the interface developed by Barlakas et al. (2022) was utilized that links the two models and supplies the bulk optical properties (gas + scattering) from ARTS into RTTOV-SCATT. In this way, there is a full consistency in the input between the models, while we avoid any other inconsistencies, e.g. vertical discretisation. For details on the interface, the reader is referred to Barlakas et al. (2022).

For simulations, both simplified (Gaussian cloud fields) and realistic profiles have been considered. However, herein, results are presented for only one profile from the IFS, corresponding to a scene at one location of the Atmospheric Infrared Sounder. For details on the dataset, the reader is referred to Barlakas et al. (2022). The profile is illustrated in Fig. 3. For simplicity, we added all frozen hydrometeors, i.e. snow, graupel, and cloud-ice (ice) into a single frozen category and a single microphysical representation was used, i.e. the large plate aggregate habit and the PSD by Field et al. (2007) (tropical configuration). In addition, a black surface is considered, i.e. surface emissivity of 1.0, since the focus of this study is the simulations over scattering media at channels with low sensitivity to surface. The default spectroscopy configuration of RTTOV has been employed (Turner et al., 2019) in both ARTS and RTTOV.

Simulations are performed on the basis of the Advanced Technology Microwave Sounder (ATMS) for frequencies between 89.0 and about 191.31 GHz over cloudy and precipitating conditions. Details on the channel characteristics of ATMS are found in Table 1. The following types of simulations are conducted:

- A pure ARO simulation by means of ARTS (reference simulation), employing the RT4 scattering solver (Evans and Stephens, 1995). Herein, 36 streams have been employed to ensure accurate radiative transfer simulations in presence

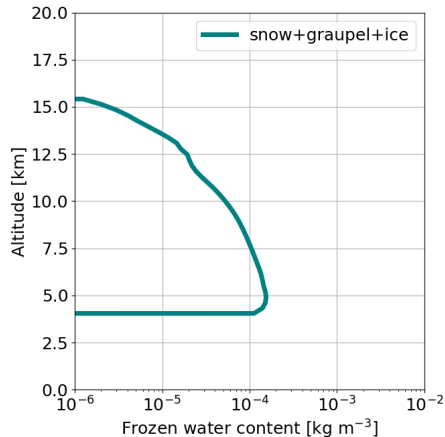


Figure 3. Example profile from the Integrated Forecast System (IFS) illustrating the combined hydrometeor water content (snow + graupel + ice).

of clouds; the larger the number of streams, the higher the accuracy. Simulations are conducted for the first two Stokes elements.

- A pure TRO simulation by means of RTTOV-SCATT v13.0; the original polarisation parameterisation by Barlakas et al. (2021) is turned off, since it is applicable only for conical scanners.
- An approximated ARO simulation (hereafter denoted as aARO) following the new parameterisation, implemented in RTTOV-SCATT.

The TRO simulation on the basis of ARTS is not presented, since the level of agreement between RTTOV-SCATT and ARTS in case of TRO has been extensively covered by Barlakas et al. (2022). For the example profile and the frequencies considered here, the differences between the models is from 0.1 K (at nadir) to about 1.2 K (at 75 °); the differences increase with increasing θ_{inc} .

5 Results

The performance of the polarisation parameterisation by means of the ATMS channels no. 16–22 is highlighted in Fig. 4. Results are presented by means of the hydrometeor impact:

$$\Delta T_B = T_{B,\text{cloudy}} - T_{B,\text{clear}}, \quad (17)$$

where $T_{B,\text{cloudy}}$ denotes the brightness temperature for the cloudy and precipitating column, while $T_{B,\text{clear}}$ is the corresponding clear sky counterpart.

Table 1. Channel characteristics of the Advanced Technology Microwave Sounder (ATMS).

Frequency[GHz]	Channel no.	Polarisation
88.20	ATMS-16	QV
165.50	ATMS-17	QH
183.31±7.0	ATMS-18	QH
183.31±4.5	ATMS-19	QH
183.31±3.0	ATMS-20	QH
183.31±1.8	ATMS-21	QH
183.31±1.0	ATMS-22	QH

To begin with, at exactly $\theta_{\text{inc}} = 0^\circ$ (nadir), ARO hydrometeors are characterised by the same extinction and asymmetry parameter at both V- and H-polarisation, i.e. $K_V = K_H$ and $g_V = g_H$. This means that the brightness temperature difference between V- and H-channels, i.e. the polarisation difference (PD = $T_{B,V} - T_{B,H}$), is zero. Although the polarisation signal is zero, there are still large differences at nadir between TRO and ARO (see all panels of Fig. 4). This is attributed to the smaller g and larger K of ARO compared to TRO hydrometeors (see Fig. 2a, b, d, and e) at $\theta_{\text{inc}} = 0$ (and values close to nadir), resulting in larger ΔT_B values; the differences in ΔT_B between TRO and ARO can be up to 8 K (see Fig. 4c).

The existing RTTOV-SCATT framework (in black; TRO), largely underestimates ΔT_B of ARO up to θ_{inc} of about 50° . Further increasing θ_{inc} leads to an overestimation of ΔT_B that can yield differences of about 5 K for zenith angles out to 65° , depending on the cloud amount and the channel sensitivity to cloud and precipitation; the larger the cloud amount (and the channel sensitivity), the larger the differences between the ARO and TRO. These differences are simply because TRO hydrometeors produce only limited polarisation (no dichroism effect), their bulk properties are completely different to the ARO counterpart (even when polarisation is close to zero, i.e. at nadir), while the current RTTOV-SCATT version does not vary the optical properties with the rotation of polarisation with the scan angle of the sensor.

On the contrary, our polarisation parameterisation (aARO) provides realistic simulations of the ARO behavior. Not only does it give a good representation of the bulk signature of ARO hydrometeors close to nadir, but it also follows the special patterns that are evident in the high peaking channels at the highest earth incident angles, i.e. ATMS channel no. 20–22. Overall, the new parameterisation leads to a significant improvement, especially out to 55° , reducing error in ΔT_B by up to about 8 K.

6 Implications for conical scanning radiometers

Although the new parameterisation has been motivated by the need to support cross-track scanners, the 4D LUT is also applicable to conical scanning radiometers. The performance of the new scheme (in this section referred to as aARO-new) compared to the old scheme (constant scaling factor; hereafter referred to as aARO-old, Barlakas et al., 2021) is highlighted in Fig. 5. Simulations are conducted for two frequencies, i.e. 88.2 and 166.5 GHz. Accordingly, the results should be considered relevant to all conical scanners equipped with similar frequencies, e.g. the Advanced Microwave Scanning Radiometer-2 (AMSR-2),

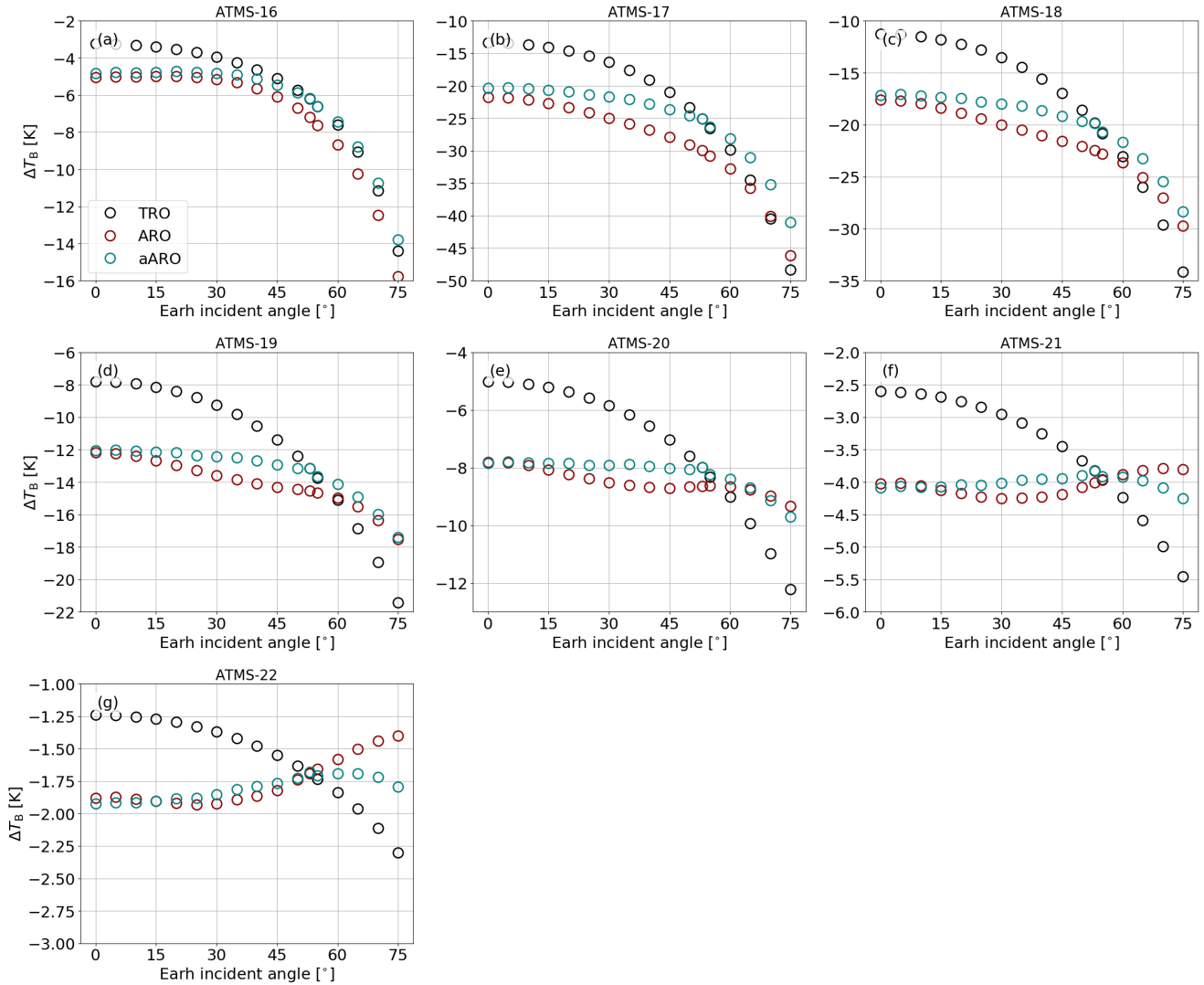


Figure 4. For the example profile (see Fig. 3), hydrometeor impact, i.e. $\Delta T_B = T_{B,\text{cloudy}} - T_{B,\text{clear}}$, as function of the Earth incident angle resulted from ARO, TRO, and the approximated ARO (aARO) simulations. Results are presented for the frequencies between 89.0 and about 191.31 GHz from the Advanced Technology Microwave Sounder (ATMS)

the Global Precipitation Measurement Microwave Imager (GMI), and the Special Sensor Microwave Imager Sounder (SSMIS).

The old parameterisation, which is valid only for conical scanners (about 55°), is described by a single scaling factor (16%, i.e. a polarisation ratio of 1.4) that is applied to all frequencies. Consequently, the resulting aARO-V-old and aARO-H-old are always symmetric with respect to the TRO value. Although the old scheme does a reasonable job in reproducing the observed

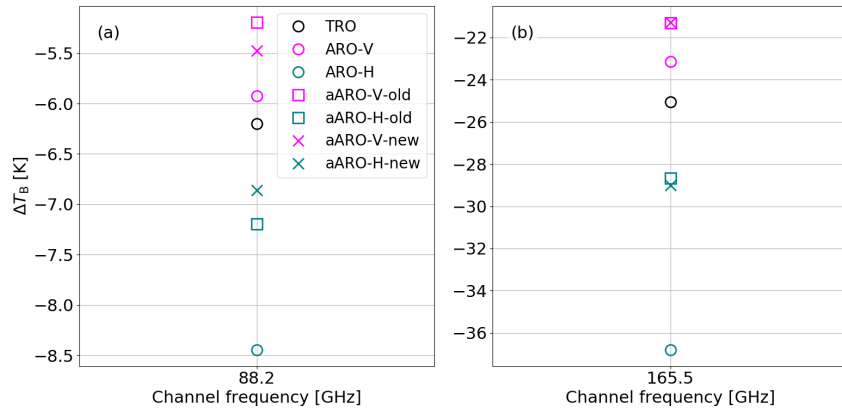


Figure 5. For the example profile (see Fig. 3), hydrometeor impact, i.e. $\Delta T_B = T_{B,\text{cloudy}} - T_{B,\text{clear}}$ as simulated in case of conical scanning radiometers equipped with frequencies of about (a) 88.2 GHz and (b) 166.5 GHz. Results are presented for ARO, the old parameterisation (aARO-old, Barlakas et al., 2021), and for the new parameterisation for both V- and H-polarisation, and TRO.

polarised scattering, the latter behaviour is not entirely true. From the ARO simulations, it is now clear that ARO-V is much closer to TRO compared to ARO-H. This behaviour likely comes from the asymmetries in V- and H- extinction that are shown in Figure 3 and are present even at 55° . Hence, the scaling that needs to be applied to H-channels should be larger than the one at V-channels and this needs to vary with frequency. The new parameterisation should provide a better representation of this behaviour. In the example of Figure 5, there is no clear evidence which scheme performs best. Recall here that the old scheme uses the same scaling factor under all conditions ($\rho = 1.4$ is translated to a scaling of about 16.7%), e.g. cloud amount and frequencies. In the particular example, this single scaling matches better the mean bulk properties at H- and V-polarisation. However, based on other cloud profiles, the new scheme should in general outperform the old one, since it will represent better the mean optical properties. This will be further assessed by means of passive monitoring assimilation experiments.

7 Conclusions and future work

In this mission, an effort has been conducted to further improve the physical representation of polarised scattering within the Radiative Transfer model for TOVS that accounts for multiple scattering (RTTOV-SCATT).

To model the effect of azimuthally randomly oriented (ARO) frozen hydrometeors and recreating the observed polarisation signal from cross-track scanners (including the rotation of polarisation with scan angle in case of cross-track scanners) a frequency-, temperature-, angular-, and water content-dependent scaling factor is prescribed. The scaling factor is the ratio of the bulk properties between ARO and TRO (totally randomly oriented) hydrometeors. For the ARO hydrometeors, the large plate aggregate habit for a tilt angle of 0° and the particle size distribution (PSD) of Field et al. (2007) (tropical configuration) are employed. In the framework of RTTOV-SCATT, the new parameterisation is implemented on the basis of a four-dimensional (4D) lookup tables (LUT) that is applied to the layer bulk scattering properties of TRO hydrometeors. Note here that the scheme

requires a rather minor adaption of software, while it adds only limited calculation burden; limited to the ingestion of the LUT (including any interpolations), the LUT search, and the scaling of the TRO properties.

The scheme was validated against the Atmospheric Radiative Transfer Simulator (ARTS) for ARO simulations on the basis of the high frequency channels of the Advanced Technology Microwave Sounder (ATMS), i.e. 89.0–191.31 GHz. With the new framework, RTTOV-SCATT is able to realistically simulate the effect of preferentially oriented frozen hydrometeors and leads to a significant improvement, especially at Earth incident angles close to nadir; it diminishes maximum modelling errors up to about 8 K. The applicability of the new scheme to conical scanning radiometers has been also successfully tested. The new scheme provides more realistic simulations of preferentially oriented hydrometeors.

A key aspect of this scheme is its high flexibility: based on optical properties from a scattering database (Brath et al., 2020) and being frequency-dependent imply that the scheme will be relatively straightforward to adapt when more oriented hydrometeors (scattering databases) and sub-millimetre observations from the upcoming Ice Cloud Imager (ICI) mission will be available. This scheme should bring the operational RTTOV-SCATT solver one step closer to a more complete representation of polarised scattering, improving simulations for observations from all microwave radiometers, which could potentially improve weather forecasting.

The new scheme will be made available in the upcoming RTTOV v13.2 release (in late 2022). It is still to be decided whether the new scheme will become the default, and/or whether there might be different recommended defaults for cross-track and conical scanning radiometers. These questions will be decided based on testing of the new scheme within the Integrated Forecast System (IFS) of the European Centre for Medium-Range Weather Forecasts (ECMWF) by means of passive monitoring and active assimilation experiments. This will compare the ability of the ARO scheme to simulate brightness temperatures from all the cross track scanners that are currently used in all-sky assimilation, e.g. the Advanced Microwave Sounding Unit-A and the Microwave Humidity Sounder. A future step would be to explore the performance of the scheme for radar backscattering. A final question that will need future work is whether it may be necessary to use different optical properties for the delta-Eddington scattering solver in RTTOV-SCATT (which considers all angles of radiation) compared to the final line-of-sight integration, where the incident angle of the observation and the scattering incident angle (θ_{inc}) are always identical.

Appendix A: A generalised approach for pure V- and H-polarisation

The traditional approach to view polarisation dates back to Stokes (1860). He uncovered that the polarisation of the electromagnetic (EM) radiation can be described by real observables. This yield the Stokes vector comprised by four parameters:

$$\mathbf{S} = \begin{bmatrix} I \\ Q \\ U \\ V \end{bmatrix}, \quad (\text{A1})$$

each of them holding the units of irradiance (W m^{-2}) Stokes (1860): I is the total irradiance, Q and U denote linear polarisation, while V describes circular polarisation Stokes (1860).

In microwave remote sensing a widely used framework for describing EM radiation is by means of the modified Stokes vector (Piepmeier et al., 2008). This is described as follows:

$$\mathbf{m} = \begin{bmatrix} I_V \\ I_H \\ U \\ V \end{bmatrix}, \quad (\text{A2})$$

where I_V and I_H , is the irradiance at V- and H- polarisation. With this formalism, one can also express the corresponding modified Stokes brightness temperature.

A Stoke vector is converted to its modified counterpart by the the matrix:

$$\mathbf{C}_m = \begin{bmatrix} 1/2 & 1/2 & 0 & 0 \\ 1/2 & -1/2 & 0 & 0 \\ 0 & 0 & 1 & 0 \\ 0 & 0 & 0 & 1 \end{bmatrix}. \quad (\text{A3})$$

The reversed transformation is:

$$\mathbf{C}_s = \begin{bmatrix} 1 & 1 & 0 & 0 \\ 1 & -1 & 0 & 0 \\ 0 & 0 & 1 & 0 \\ 0 & 0 & 0 & 1 \end{bmatrix}. \quad (\text{A4})$$

One way to look at scalar radiative transfer theory is by keeping track of either the first or second element of the modified Stokes vector. The extinction expressed by means of the modified Stokes vector can be written as:

$$\mathbf{K}_m = \mathbf{C}_m \mathbf{K} \mathbf{C}_s = \begin{bmatrix} K_{11} + K_{12} & 0 & 0 & 0 \\ 0 & K_{11} - K_{12} & 0 & 0 \\ 0 & 0 & K_{11} & K_{34} \\ 0 & 0 & -K_{34} & K_{11} \end{bmatrix}, \quad (\text{A5})$$

where \mathbf{K} is taken from Eq. (8). The elements 11 and 22 of A5 correspond to the extinction at pure V- and H-polarisation respectively, i.e. K_V and K_H . The fact that the 12 and 21 elements are zero points to the fact that extinction does not blend V- and H-polarisations. To highlight, considering incoming EM radiation with no preferred polarisation, i.e. extraterrestrial radiation entering the top of the atmosphere, $\mathbf{m} = [1 \ 1 \ 0 \ 0]^T$, we end up with the following formalism:

$$\mathbf{K}_m \mathbf{m} = \begin{bmatrix} K_V \\ K_H \\ 0 \\ 0 \end{bmatrix} = \begin{bmatrix} K_{11} + K_{12} \\ K_{11} - K_{12} \\ 0 \\ 0 \end{bmatrix} \quad (\text{A6})$$

The same approach can be applied to the scattering matrix:

$$\mathbf{Z}_m \mathbf{m} = \mathbf{C}_m \mathbf{Z} \mathbf{C}_s \mathbf{m} = \begin{bmatrix} Z_{11} + Z_{21} \\ Z_{11} - Z_{21} \\ 2Z_{31} \\ 2Z_{41} \end{bmatrix}, \quad (\text{A7})$$

where \mathbf{Z} is given by Eq. (1). Compared to Eq. (A5), the expression for scattering matrix is more complicated, on the grounds that Eq. (A7) is non-diagonal. This means that different polarisation components will be mixed by scattering. Nonetheless, the scattering matrix for pure V- and H-polarisation is given by,

$$\begin{aligned} Z_V &= Z_{11} + Z_{21}, \\ Z_H &= Z_{11} - Z_{21}. \end{aligned} \quad (\text{A8})$$

From this expression, one can derive the asymmetry parameter for pure V- and H-polarisation in case of ARO following Eq. (9). Note here that this expression is valid only for non-nadir geometries, since polarisation is negligible at exact nadir view (see Section 5). At nadir, $g_V = g_H$ and the ARO asymmetry parameter is derived via Eq. (9). Similarly, the single scattering albedo at pure V- and H-polarisation can be derived from Eq. (13) following Eqs. (A8) and (A6).

Finally, we should comment that the derivation of g_V and g_H on the basis of preferentially oriented hydrometeors is yet not fully clear. So far, only limited work has been conducted, and to the majority, it is limited to theoretical reviews (Piepmeier et al., 2008). The above expression (Eq. A7), points that scattering leads to a blended of different polarisation components. Going even further, the way to handle this problem within a radiative transfer modeling framework, increases the level of complexity, since it is unclear how to treat the bulk optical properties for the full-scattering calculation (where all directions of radiation may be relevant).

References

- Barlakas, V.: A new three-dimensional vector radiative transfer model and applications to Saharan dust fields, Ph.D. thesis, <https://nbn-resolving.org/urn:nbn:de:bsz:15-qucosa-207467>, 2016.
- Barlakas, V., Macke, A., and Wendisch, M.: SPARTA – Solver for Polarized Atmospheric Radiative Transfer Applications: Introduction and application to Saharan dust fields, *J. Quant. Spectrosc. Radiat. Transfer*, 178, 77–92, <https://doi.org/10.1016/j.jqsrt.2016.02.019>, electromagnetic and light scattering by nonspherical particles XV: Celebrating 150 years of Maxwell’s electromagnetics, 2016a.
- Barlakas, V., Geer, A. J., and Eriksson, P.: Introducing hydrometeor orientation into all-sky microwave and submillimeter assimilation, *Atmos. Meas. Tech.*, 14, 3427–3447, <https://doi.org/10.5194/amt-14-3427-2021>, 2021.
- Barlakas, V., Galligani, V. S., Geer, A. J., and Eriksson, P.: On the accuracy of RTTOV-SCATT for radiative transfer at all-sky microwave and submillimeter frequencies, *J. Quant. Spectrosc. Radiat. Transf.*, 283, 108–137, <https://doi.org/10.1016/j.jqsrt.2022.108137>, 2022.
- Bauer, P., Moreau, E., Chevallier, F., and O’keeffe, U.: Multiple-scattering microwave radiative transfer for data assimilation applications, *Q. J. R. Meteorol. Soc.*, 132, 1259–1281, <https://doi.org/10.1256/qj.05.153>, 2006.
- Brath, M., Ekelund, R., Eriksson, P., Lemke, O., and Buehler, S. A.: Microwave and submillimeter wave scattering of oriented ice particles, *Atmos. Meas. Tech.*, 13, 2309–2333, <https://doi.org/10.5194/amt-13-2309-2020>, 2020.
- Buehler, S., Eriksson, P., Kuhn, T., von Engeln, A., and Verdes, C.: ARTS, the atmospheric radiative transfer simulator, *J. Quant. Spectrosc. Radiat. Transfer*, 91, 65–93, <https://doi.org/https://doi.org/10.1016/j.jqsrt.2004.05.051>, 2005.
- Davis, C. P., Wu, D. L., Emde, C., Jiang, J. H., Cofield, R. E., and Harwood, R. S.: Cirrus induced polarization in 122 GHz aura Microwave Limb Sounder radiances, *Geophys. Res. Lett.*, 32, <https://doi.org/10.1029/2005GL022681>, 2005.
- Emde, C., Buehler, S. A., Davis, C., Eriksson, P., Sreekha, T. R., and Teichmann, C.: A polarized discrete ordinate scattering model for simulations of limb and nadir long-wave measurements in 1-D/3-D spherical atmospheres, *J. Geophys. Res.*, 109, <https://doi.org/10.1029/2004JD005140>, 2004.
- Eriksson, P., Ekelund, R., Mendrok, J., Brath, M., Lemke, O., and Buehler, S. A.: A general database of hydrometeor single scattering properties at microwave and sub-millimetre wavelengths, *Earth Syst. Sci. Data*, 10, 1301–1326, <https://doi.org/10.5194/essd-10-1301-2018>, 2018.
- Evans, K. F. and Stephens, G. L.: Microwave radiative transfer through clouds composed of realistically shaped ice crystals. Part II. Remote sensing of ice clouds, *J. Atmos. Sci.*, 52, 2058–2072, [https://doi.org/10.1175/1520-0469\(1995\)052<2058:MRTTCC>2.0.CO;2](https://doi.org/10.1175/1520-0469(1995)052<2058:MRTTCC>2.0.CO;2), 1995.
- Field, P. R., Heymsfield, A. J., and Bansemir, A.: Snow size distribution parameterization for midlatitude and tropical ice clouds, *J. Atmos. Sci.*, 64, 4346–4365, <https://doi.org/10.1175/2007JAS2344.1>, 2007.
- Forbes, R., Geer, A. J., Lonitz, K., and Ahlgrimm, M.: Reducing systematic errors in cold-air outbreaks, pp. 17–22, <https://doi.org/10.21957/s41h7q7l>, 2016.
- Galligani, V. S., Wang, D., Corrales, P. B., and Prigent, C.: A parameterization of the cloud scattering polarization signal derived from GPM observations for microwave fast radiative transfer models, *IEEE Trans. Geosci. Remote Sens.*, pp. 1–10, <https://doi.org/10.1109/TGRS.2021.3049921>, 2021.
- Geer, A. J.: Physical characteristics of frozen hydrometeors inferred with parameter estimation, *Atmos. Meas. Tech. Discuss.*, 2021, 1–40, <https://doi.org/10.5194/amt-2021-50>, 2021.

- Geer, A. J., Baordo, F., Bormann, N., Chambon, P., English, S. J., Kazumori, M., Lawrence, H., Lean, P., Lonitz, K., and Lupu, C.: The growing impact of satellite observations sensitive to humidity, cloud and precipitation, *Quart. J. Roy. Meteorol. Soc.*, 143, 3189–3206, <https://doi.org/10.1002/qj.3172>, 2017.
- Geer, A. J., Bauer, P., Lonitz, K., Barlakas, V., Eriksson, P., Mendrok, J., Doherty, A., Hocking, J., and Chambon, P.: Bulk hydrometeor optical properties for microwave and sub-millimetre radiative transfer in RTTOV-SCATT v13.0, *Geosci. Model Dev.*, 14, 7497–7526, <https://doi.org/10.5194/gmd-14-7497-2021>, 2021.
- Gong, J. and Wu, D. L.: Microphysical properties of frozen particles inferred from Global Precipitation Measurement (GPM) Microwave Imager (GMI) polarimetric measurements, *Atmos. Chem. Phys.*, 17, 2741–2757, <https://doi.org/10.5194/acp-17-2741-2017>, 2017.
- Kaur, I., Eriksson, P., Barlakas, V., Pfreundschuh, S., and Fox, S.: Fast Radiative Transfer Approximating Ice Hydrometeor Orientation and Its Implication on IWP Retrievals, *Remote Sens.*, 14, <https://doi.org/10.3390/rs14071594>, 2022.
- Khvorostyanov, V. I. and Curry, J. A.: *Thermodynamics, kinetics, and microphysics of clouds*, Cambridge University Press, <https://doi.org/10.1017/CBO9781139060004>, 2014.
- Mishchenko, M., Hovenier, J., and Travis, L.: *Light scattering by nonspherical particles: theory, measurements, and applications*, Elsevier Science, 1999.
- Mishchenko, M. I. and Yurkin, M. A.: On the concept of random orientation in far-field electromagnetic scattering by nonspherical particles, *Opt. Lett.*, 42, 494–497, <https://doi.org/10.1364/OL.42.000494>, 2017.
- Piepmeyer, J. R., Long, D. G., and Njoku, E. G.: Stokes Antenna Temperatures, *IEEE T. Geosci. Remote*, 46, 516–527, <https://doi.org/10.1109/TGRS.2007.909597>, 2008.
- Saito, M. and Yang, P.: Oriented Ice Crystals: A Single-Scattering Property Database for Applications to Lidar and Optical Phenomenon Simulations, *J. Atmos. Sci.*, 76, 2635–2652, <https://doi.org/10.1175/JAS-D-19-0031.1>, 2019.
- Saunders, R., Hocking, J., Turner, E., Rayer, P., Rundle, D., Brunel, P., Vidot, J., Roquet, P., Matricardi, M., Geer, A., Bormann, N., and Lupu, C.: An update on the RTTOV fast radiative transfer model (currently at version 12), *Geosci. Model Dev.*, 11, 2717–2737, <https://doi.org/10.5194/gmd-11-2717-2018>, 2018.
- Stokes, G. G.: On the intensity of the light reflected from or transmitted through a pole of plates, vol. 11, *Proc. R. Soc. London*, <https://doi.org/doi.org/10.1098/rspl.1860.0119>, 1860.
- Teichmann, C., Buehler, S., and Emde, C.: Understanding the polarization signal of spherical particles for microwave limb radiances, *J. Quant. Spectrosc. Radiat. Transfer*, 101, 179–190, <https://doi.org/10.1016/j.jqsrt.2006.03.001>, 2006.
- Turner, E., Rayer, P., and Saunders, R.: AMSUTRAN: A microwave transmittance code for satellite remote sensing, *J. Quant. Spectrosc. Radiat. Transf.*, 227, 117–129, <https://doi.org/https://doi.org/10.1016/j.jqsrt.2019.02.013>, 2019.